

INTERMEDIATE-VELOCITY GAS IN THE CANADIAN GALACTIC PLANE SURVEY

C. R. KERTON

Department of Physics and Astronomy, Iowa State University, Ames, IA 50011; kerton@iastate.edu

LEWIS B. G. KNEE

Millimetre Astronomy Group, Herzberg Institute of Astrophysics, National Research Council of Canada,
5071 West Saanich Road, Victoria, BC V9E 2E7, Canada; lewis.knee@nrc-cnrc.gc.ca

AND

ANDREW J. SCHAEFFER

Department of Earth and Ocean Sciences, University of British Columbia, 6339 Stores Road,
Vancouver, BC V6T 1Z4, Canada; aschaeffer@eos.ubc.ca

Received 2005 August 17; accepted 2005 November 26

ABSTRACT

We present observations of intermediate-velocity clouds (IVCs) found at positive velocities in the Canadian Galactic Plane Survey Phase I region ($74^\circ < l < 148^\circ$, $-3.5^\circ < b < +5.6^\circ$). A catalog of 138 distinct IVCs and 13 IVC complexes has been compiled. From the global characteristics of our sample we demonstrate that the majority of these IVCs are directly associated with energetic phenomena, such as supernova explosions and massive star-forming regions, within the disk of the Galaxy and thus form a different population than the high-velocity clouds and high-latitude IVCs. We report what we believe to be the first detection of H I 21 cm absorption of a background source by an IVC and attempt to determine its physical properties and distance. We discuss in some detail a few of the IVCs that illustrate the connection between the clouds and energetic phenomena in the Galaxy. We suggest that the velocity shift of these IVCs away from the bulk of the Galactic H I emission provides an opportunity to study the structure of the low-latitude H I emission in a relatively confusion-free environment and present two examples of large (degree-scale) complexes of H I emission particularly suitable for such studies.

Key words: Galaxy: structure — ISM: clouds — ISM: structure — radio lines: ISM — surveys

Online material: machine-readable table

1. INTRODUCTION

Much of the 21 cm H I line emission from our Galaxy is observed to have velocities relative to the local standard of rest (V_{LSR}) consistent with simple kinematic models for the motion of gas in our Galaxy. For example, in the second quadrant of the Galaxy ($90^\circ \leq l \leq 180^\circ$) a flat rotation curve model with $R_\odot = 8.5$ kpc, $V_\odot = 220$ km s $^{-1}$, and a maximum galactocentric radius of 30 kpc predicts that the bulk of the H I emission observed should fall within the velocity range -120 km s $^{-1} < V_{\text{LSR}} < 0$ km s $^{-1}$. A cursory examination of an H I position-velocity data cube will show that this is indeed the case. However, given sufficiently sensitive observations, one can find regions of emission that clearly lie outside of the “allowed” range of velocities. Such H I-emitting regions are called intermediate- or high-velocity clouds (IVCs or HVCs, respectively), depending on the degree to which their observed velocity differs from the maximum (or minimum) allowed velocity for a given kinematic model. Following Wakker (1991), we use the deviation velocity V_{dev} as the criterion for identifying gas with peculiar velocities and define an IVC as a cloud with deviation velocity ($V_{\text{dev}} \equiv V_{\text{LSR}} - V_{\text{max}}$; this is the appropriate definition for the clouds in this paper, which have $V_{\text{LSR}} > 0$) between +10 and +90 km s $^{-1}$, where V_{LSR} is the observed IVC velocity and V_{max} is the maximum allowed velocity from the simple kinematic model. The lower (+10 km s $^{-1}$) limit accounts for the velocity dispersion expected for typical Galactic H I, and the upper (+90 km s $^{-1}$) limit is the demarcation velocity between IVCs and HVCs suggested by Wakker (2004).

While observationally IVCs are just lower velocity counterparts of HVCs, these objects, in some part, represent different

populations. Many HVCs appear to represent an extragalactic population that consists of infalling gas from tidally disrupted satellite galaxies and perhaps even more primordial infalling material (e.g., Putman & Moore 2002). In contrast, at least some IVCs are probably associated with energetic phenomena within our Galaxy, such as supernova explosions and stellar winds, and on a larger scale are thus related to the circulation of material between the disk and halo of our Galaxy. Whether some HVCs are also related to this “Galactic fountain” is still a matter of much debate. Considering that much of the structure of the interstellar medium (ISM) is shaped through the collective action of energetic phenomena, many IVCs may differ from the general neutral ISM only in their velocity shift away from the bulk of the emission. In this light IVCs provide us with the opportunity to view the basic structure of the ISM in a relatively clear way.

In this paper we present H I 21 cm line observations of IVCs located within the Canadian Galactic Plane Survey (CGPS) Phase I region ($74^\circ < l < 148^\circ$, $-3.5^\circ < b < +5.6^\circ$). In § 2 we outline the observations and data analysis techniques. The global properties of the sample are presented and discussed in § 3. In § 4 we individually examine a number of the more notable IVCs, followed by a summary and some concluding thoughts in § 5.

2. DATA AND SEARCH TECHNIQUE

2.1. CGPS H I Mosaics

The CGPS is one part of a multinational effort to examine the various components of the ISM of our Galaxy at approximately 1' resolution. Phase I of the CGPS covered $74^\circ < l < 148^\circ$,

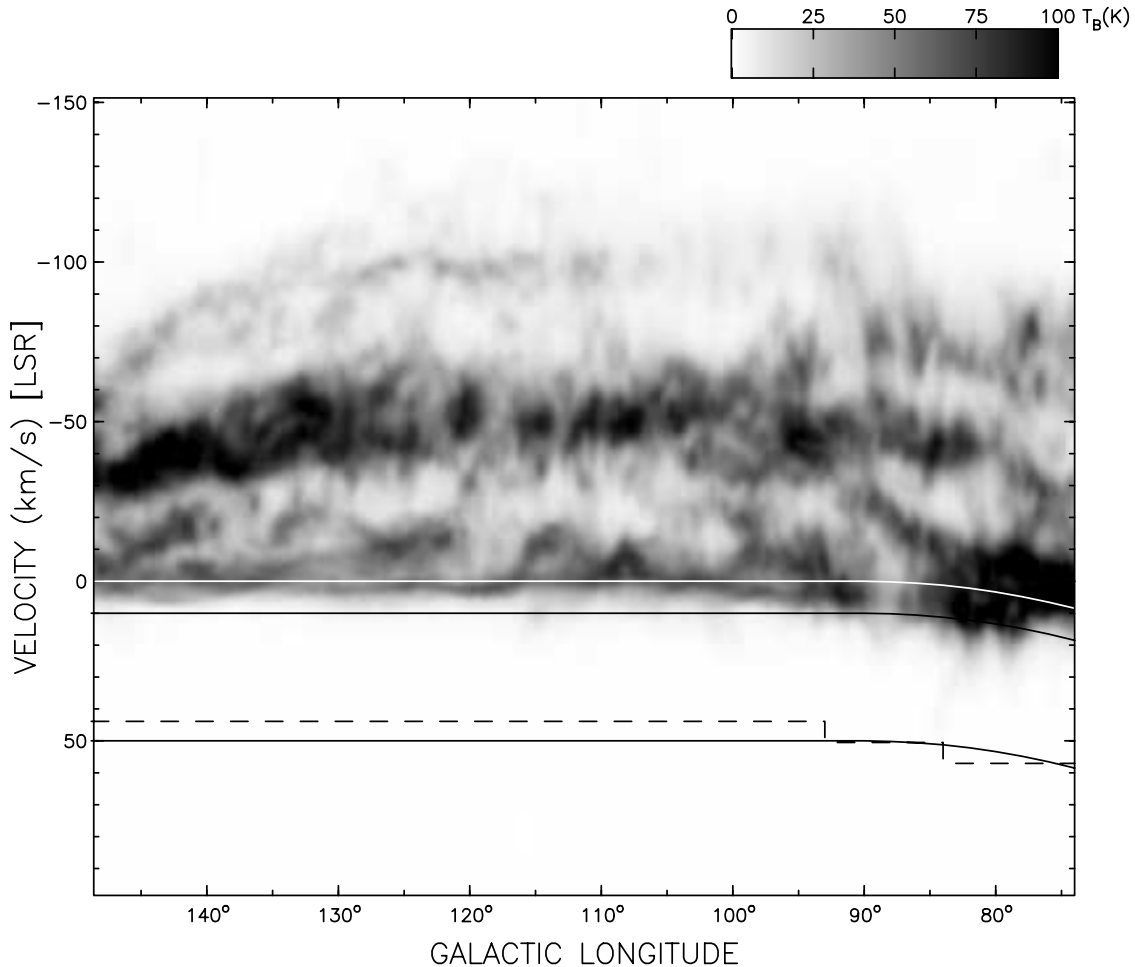


FIG. 1.—Velocity coverage for the IVC search. H I emission is shown from the LRDS at $b = 0^\circ$. The white line shows the maximum allowed velocity (V_{\max}) for a flat rotation curve model with $R_\odot = 8.5$ kpc and $V_\odot = 220$ km s $^{-1}$. The two solid black lines mark the velocity range corresponding to $+10$ km s $^{-1} \leq V_{\text{dev}} \leq +50$ km s $^{-1}$, and the dashed line shows the positive velocity limit of the CGPS in this region.

$-3.5 < b < +5.6$ and included radio continuum, molecular line, and infrared data in addition to the H I line data that we describe here. The data reduction techniques and survey methodology are described in Taylor et al. (2003), and we note that all of the CGPS data are freely available through the Canadian Astronomy Data Centre archive.

H I data for Phase I of the CGPS were obtained by the Dominion Radio Astrophysical Observatory (DRAO) Synthesis Telescope (Landecker et al. 2000) between 1995 and 2000. The DRAO Synthesis Telescope consists of seven dish antennas (five of diameter 8.5 m, two of 9.1 m) arranged along a 620 m east-west line resulting in a resolution of $\sim 1'$ and a FWHM field of view of $\sim 90'$ when operated in the 21 cm wave band. For the CGPS, observations were made with a spectrometer resolution of 1.32 km s $^{-1}$ over a bandwidth of 211 km s $^{-1}$ for a typical velocity coverage of -160 km s $^{-1} < V_{\text{LSR}} < +50$ km s $^{-1}$. The standard observing technique used at DRAO results in an essentially completely filled u - v plane for each observed field. For the CGPS, short-spacing data were added using data from the Low-Resolution DRAO Survey (LRDS) described in § 2.2. The final archived H I data product is a series of 36 overlapping 5.12×5.12 data cubes (1024×1024 18'' pixels, 0.82 km s $^{-1}$ channel spacing) covering the survey region. The rms noise in a single channel varies between 2.9 and 4.6 K in an “egg-crate” pattern determined by the overlap in the single-dish power patterns from the individual fields comprising a mosaic.

2.2. The Low-Resolution DRAO Survey

To provide short-spacing data for the DRAO interferometer H I observations, a complementary single-dish survey was undertaken using the 26 m antenna at DRAO. The resulting LRDS (Higgs & Tapping 2000) covers $72.2 < l < 149.0$, $-5.4 < b < +7.2$ at 36' resolution and 1.32 km s $^{-1}$ velocity resolution over a 420 km s $^{-1}$ bandwidth (-260 km s $^{-1} < V_{\text{LSR}} < +160$ km s $^{-1}$ velocity coverage). The single-channel rms noise is ~ 0.25 K. The survey has been corrected for stray radiation and is fully sampled spatially. For this study the LRDS data provide views of extended very low brightness emission associated with IVCs that is not clearly visible in the interferometer-based images.

2.3. Search Technique

Although the CGPS velocity coverage was designed to detect the bulk of the allowed emission in our Galaxy, it turns out to be well suited for the detection of positive velocity IVCs at velocities up to $V_{\text{dev}} \approx +50$ km s $^{-1}$. Figure 1 shows an l , v slice from the LRDS at $b = 0^\circ$. Superposed is a white line that shows the maximum allowed velocity (V_{\max}) for a flat rotation curve model with $R_\odot = 8.5$ kpc and $V_\odot = 220$ km s $^{-1}$. Note that there is clearly emission at all longitudes that is technically “forbidden” but is simply due to the intrinsic velocity dispersion of the H I. The two solid black lines demarcate the velocity range corresponding to $+10$ km s $^{-1} \leq V_{\text{dev}} \leq +50$ km s $^{-1}$, and the dashed

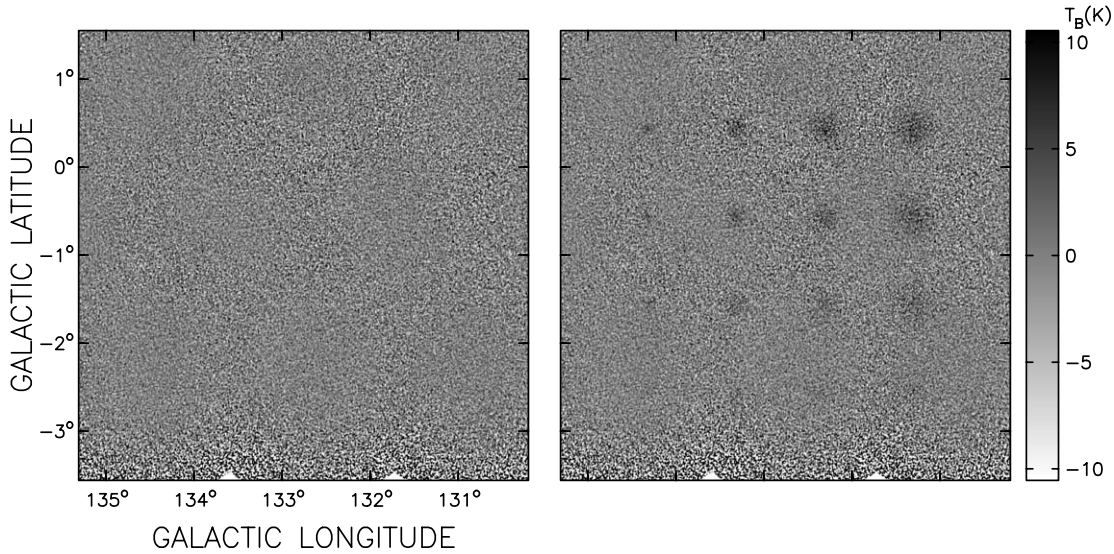


FIG. 2.—Simulated IVC grid. The left panel shows the “MY1” CGPS H I mosaic at $V_{\text{LSR}} = +26.57 \text{ km s}^{-1}$. This channel is free of emission above the noise level. The right panel shows the same channel with 16 added Gaussian IVCs with FWHMs of $5'$, $10'$, $15'$, and $20'$ (from high to low longitude) and peak brightness temperatures of 1, 2, 3, and 4 K (from low to high latitude). Note that none of the 1 K clouds are visible and that the FWHM = $5'$ clouds are at the limit of detectability.

line shows the positive velocity limit of the CGPS. As mentioned in § 1 the $+10 \text{ km s}^{-1}$ lower limit is used to avoid the majority of very low velocity emission that extends beyond V_{max} .

We examined all of the CGPS mosaics for H I emission between $V_{\text{max}} = +10 \text{ km s}^{-1}$ and the high-velocity cutoff of each mosaic. The mosaics were examined by the authors by eye at least twice in every case, both individually and as a group. For each identified IVC the l, b, v extent was noted, along with the l, b, v position of its brightest emission. For each cloud a mask was created, isolating voxels above a certain brightness temperature, which were then used to determine the average brightness of the entire cloud. Cases in which the IVC blended into the low-velocity emission or appeared to extend beyond the upper velocity cutoff of the survey were also noted.

To gain a quantitative sense of the detection limits of our sample, we added simulated Gaussian clouds (i.e., their brightness and velocity distribution are Gaussian) with varying FWHM sizes and peak brightness temperatures to channels with no apparent H I emission above the noise. These modified data cubes were then examined by eye to see which of the artificial clouds could

be recovered. Figure 2 illustrates this process. The left panel shows one of the CGPS mosaics at $V_{\text{LSR}} = +26.57 \text{ km s}^{-1}$. This channel is free of emission above the noise level. The right panel shows the same channel after we added a grid of 16 clouds with FWHMs of $5'$, $10'$, $15'$, and $20'$ (from high to low longitude) and peak brightness temperatures of 1, 2, 3, and 4 K (from low to high latitude). Examination of grids like this suggests that our inspection technique will easily recover all IVCs in the CGPS data with peak brightness temperatures above 3 K and with a size scale over $10'$. Below these limits we expect to detect only very bright small clouds or faint clouds that happen to lie in a very low noise region of the survey.

3. DETECTED IVCs AND GLOBAL PROPERTIES

We identified 138 IVCs within the survey region. A sample of the IVC catalog is presented in Table 1. Column (1) is a running identification number, and column (2) is an alternative identification in terms of Galactic longitude, latitude, and V_{LSR} . Columns (3)–(5) give the position and velocity of the maximum cloud brightness. The angular extent of the cloud is given in

TABLE 1
CGPS PHASE I POSITIVE-VELOCITY IVCs

IVC (1)	l, b, V_{LSR} ID (2)	l (deg) (3)	b (deg) (4)	V_{LSR} (km s^{-1}) (5)	l_{min} (deg) (6)	l_{max} (deg) (7)	b_{min} (deg) (8)	b_{max} (deg) (9)	$V_{\text{LSR, min}}$ (km s^{-1}) (10)	Low V^a (11)	$V_{\text{LSR, max}}$ (km s^{-1}) (12)	High V^b (13)	$T_{B, \text{avg}}$ (K) (14)
1.....	143.3–2.6+14.20	143.260	–2.610	14.20	142.760	143.590	–2.920	–2.160	10.08	1	15.85	0	5.00
2.....	145.6–0.7+16.67	145.630	–0.705	16.67	145.365	145.825	–1.235	–0.220	10.90	0	19.15	0	4.00
3.....	146.4–1.9+17.50	146.390	–1.919	17.50	146.140	146.550	–1.989	–1.829	11.73	1	19.15	0	5.00
4.....	144.6–1.5+19.97	144.625	–1.510	19.97	144.340	144.865	–1.710	–1.315	15.03	1	22.45	0	3.00
5.....	143.7+3.7+21.62	143.685	3.659	21.62	143.415	143.825	3.430	3.810	17.50	1	24.92	0	12.00
6.....	145.8+2.9+17.50	145.795	2.895	17.50	145.600	146.170	2.685	3.045	14.20	0	22.45	0	9.00
7.....	138.5–0.1+41.41	138.480	–0.130	41.41	138.405	138.490	–0.160	–0.075	10.08	0	45.53	1	26.78
8.....	141.9+4.1+09.25	141.900	4.105	9.25	141.570	142.000	4.015	4.190	7.61	1	15.03	0	8.16
9.....	141.9+1.4+10.08	141.895	1.590	10.08	141.805	141.915	1.500	1.600	6.78	1	13.38	0	21.08
10.....	136.5–0.3+40.58	136.480	–0.345	40.58	136.460	136.535	–0.380	–0.335	4.31	1	44.71	1	16.54

NOTE.—Table 1 is published in its entirety in the electronic edition of the *Astronomical Journal*. A portion is shown here for guidance regarding its form and content.
^a A “1” indicates that the IVC blends into low-velocity allowed emission.
^b A “1” indicates that the IVC extends past the high-velocity cutoff of the CGPS data.

TABLE 2
CGPS PHASE I POSITIVE-VELOCITY IVC REGIONS

Region	l_{\min} (deg)	l_{\max} (deg)	b_{\min} (deg)	b_{\max} (deg)	$V_{\text{LSR},\min}$ (km s ⁻¹)	Low V^a	$V_{\text{LSR},\max}$ (km s ⁻¹)	High V
1.....	91.790	94.390	-3.180	-1.420	16.67	0	31.52	0
2.....	91.979	92.830	2.545	2.950	15.03	1	24.09	0
3.....	89.685	89.960	2.760	3.010	12.55	1	23.67	0
4.....	88.700	90.320	0.440	1.390	12.55	1	33.16	0
5.....	82.610	83.365	-1.365	0.895	20.80	1	46.36	0
6.....	82.210	85.115	3.655	4.885	13.38	1	42.23	0
7.....	83.170	84.739	2.185	3.420	18.32	1	44.71	0
8.....	80.895	81.665	1.465	2.175	24.09	1	52.13	0
9.....	79.400	79.565	3.205	3.335	33.99	0	41.41	0
10.....	75.325	76.375	-0.115	1.295	23.27	1	55.42	0
11.....	78.550	79.155	0.230	0.585	22.45	1	53.78	0
12.....	77.010	77.550	-3.325	-2.995	23.27	1	34.81	0
13.....	76.900	78.695	1.745	3.595	21.62	1	47.18	0

^a A “1” indicates that the IVCs blend into low-velocity allowed emission.

columns (6)–(9). The minimum and maximum velocity of the cloud emission are listed in columns (10) and (12). Flags indicating whether the emission blends with local emission or extends past the high-velocity cutoff are given in columns (11) and (13). Finally, column (14) is the average brightness temperature of the cloud. In addition to the individual clouds, we also defined 13 complexes listed in Table 2. These are regions where there are a large number of apparently related IVCs or cases in which the emission structure was sufficiently complex that individual cloud identification was difficult.

In this section we first present the global properties of the IVC sample then discuss what these global properties tell us about the IVCs. Except when otherwise indicated the discussion in this section refers to the 138 individual IVCs, and we defer a discussion of the morphology and structure of individual clouds until § 4, when we examine a number of particular IVCs in more detail.

3.1. Velocity-Space Distribution

Figure 3 shows the distribution of clouds as a function of their deviation velocity. As can be seen by the cumulative distribution, also shown in the figure, the majority of the IVCs have $V_{\text{dev}} < +20$ km s⁻¹, and 75% of the sample have $V_{\text{dev}} \leq +25$ km s⁻¹.

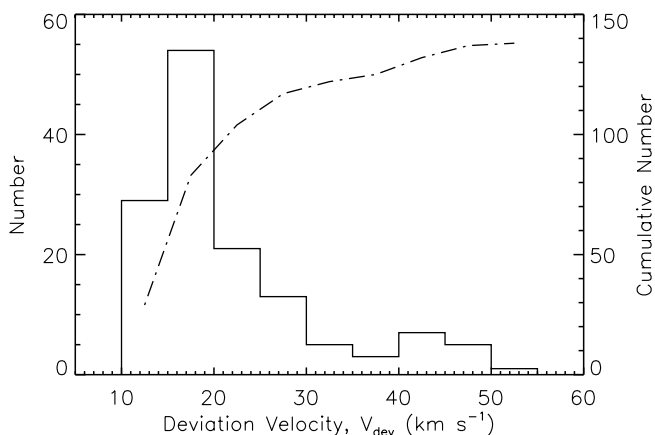


FIG. 3.—Deviation velocity distribution. The histogram shows the deviation velocity (V_{dev}) in 5 km s⁻¹ bins (*left axis*). The cumulative number distribution (*right axis*) is shown by the dot-dashed line. Note that the majority of the IVCs have $V_{\text{dev}} \leq +20$ km s⁻¹.

Of the complete sample, 83 IVCs were observed to merge into the local allowed H I emission. In these cases the $V_{\text{LSR},\min}$ in Table 1 represents the lowest velocity at which the IVC was visible as a distinct structure. In contrast, only six of the IVCs apparently extend beyond the high-velocity limit of the CGPS, and only two have emission extending throughout the entire positive velocity region. In these cases the $V_{\text{LSR},\max}$ in Table 1 represents the maximum velocity observable in that particular part of the survey. The remaining 47 IVCs are kinematically distinct, meaning that their emission disappears before both the high-velocity cutoff and the appearance of local emission. Figure 4 shows spatially averaged spectra of three IVCs that illustrate these different phenomenological types. Baselines for each spectrum are shown by the dashed line and have been offset by -130 K for IVC 96 (IVC 87.6+3.0+26.57) and by $+70$ K for IVC 26 (IVC 115.0–0.4+12.55). In all three cases one can see that there is emission that extends beyond the formal limit of $V_{\text{max}} \sim 0$ km s⁻¹ to around $V_{\text{LSR}} \sim +10$ km s⁻¹. IVC 96 is an example of a kinematically

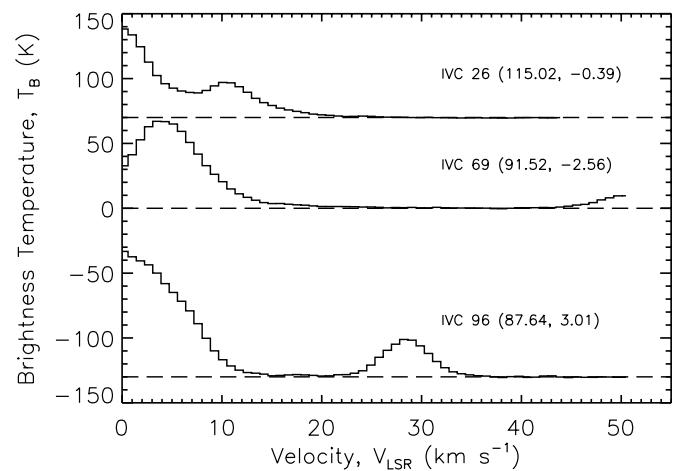


FIG. 4.—Representative IVC spectra. Three basic types of IVC spectra were observed in our sample (see text). IVC 26 (*top*) is an example of an IVC in which the low-velocity wing of the emission is blended with the bulk low-velocity emission from the Galaxy. IVC 69 (*middle*) has emission that is clearly rising through the high-velocity cutoff of the CGPS data. Finally, IVC 96 (*bottom*) illustrates a kinematically distinct spectrum. Spectra were averaged over the spatial extent of each cloud. For each spectrum the baseline is shown as a dashed line with offsets of $+70$, 0 , and -130 km s⁻¹ for IVC 26, IVC 69, and IVC 96, respectively.

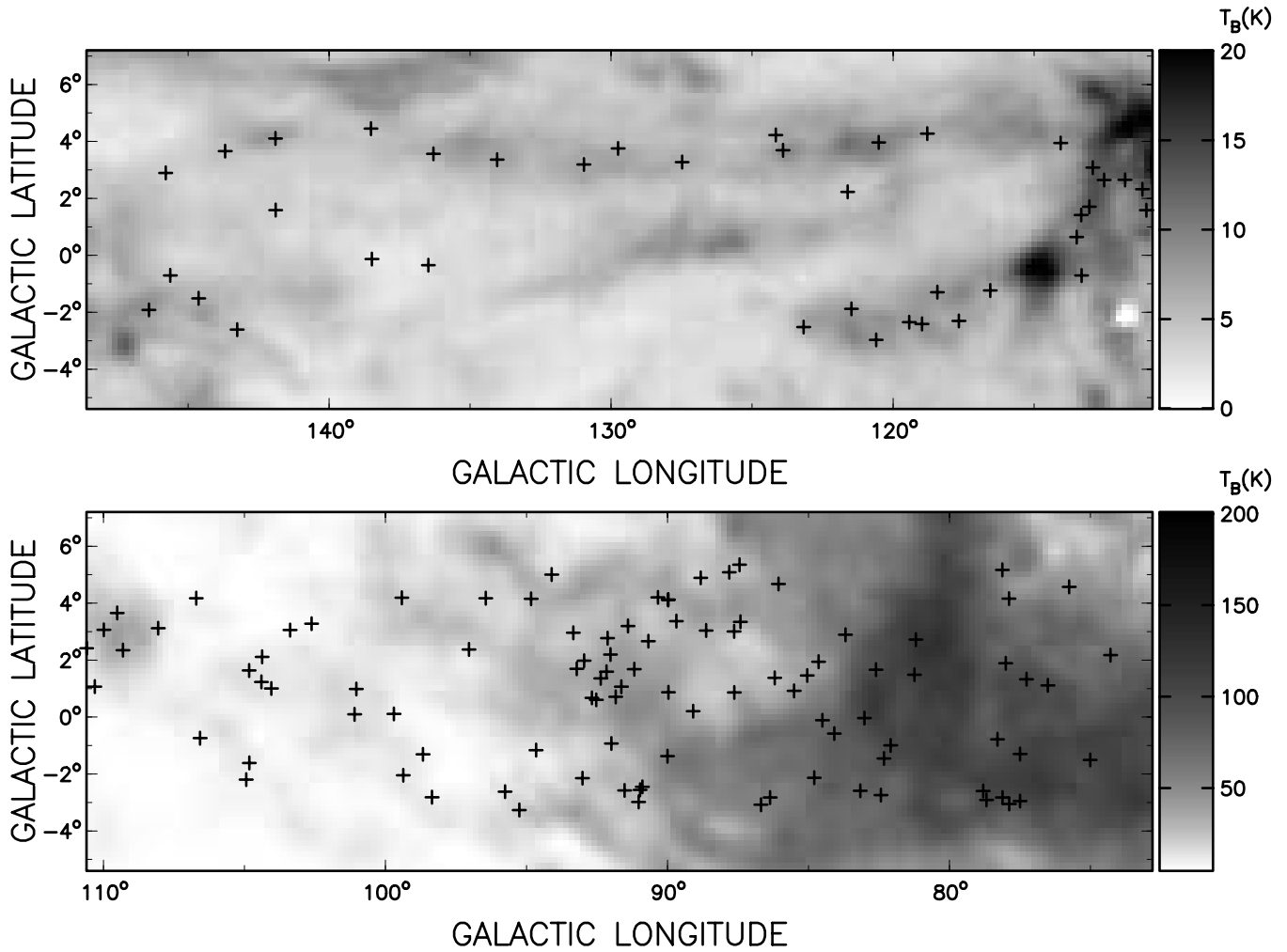


FIG. 5.—The l, b distribution of IVCs. The positions of the IVCs are indicated by the crosses. The background image is from the LRDS at $V_{\text{LSR}} = +9.36 \text{ km s}^{-1}$ from 148.6 to 110.8 (top) and from 110.6 to 74 (bottom). Note the different gray scales used in each panel and that the LRDS has a slightly larger latitude and longitude coverage than the interferometric survey data.

distinct IVC whose emission is clearly separated from the bulk of the allowed Galactic H I emission. In contrast, the lower velocity wing of emission from IVC 26 is blended with the low-velocity allowed emission. Finally, IVC 69 (IVC $91.5-2.6+49.65$) is shown to illustrate the much less common case of emission that clearly extends beyond the high-velocity cutoff of the survey.

3.2. Spatial Distribution

Figure 5 shows the distribution of the detected IVCs over the entire survey overlaid on a channel map from the LRDS at $+9.36 \text{ km s}^{-1}$. It is immediately apparent that the distribution of IVCs is not uniform across the survey region. Figure 6 is a histogram showing the number of IVCs as a function of longitude (in 5° bins) along with a cumulative distribution (dot-dashed line, right axis). We find that the majority of the IVCs (58%) are found at $l \leq 95^\circ$, and we note that all of the IVC complexes we found are at longitudes $l < 100^\circ$. In Figure 7 we have divided our sample into two parts. The top histogram shows the distribution of IVCs that merge into the allowed Galactic H I emission, and the bottom histogram shows the distribution of isolated IVCs. The distribution of the merging IVCs is fairly uniform over the entire survey region, while in contrast there is a substantial increase in the relative numbers of isolated IVCs as longitudes drop below $l = 95^\circ$. For $l > 95^\circ$ merging IVCs outnumber isolated IVCs by

more than a factor of 4 (52 vs. 12), but for $l < 95^\circ$ the numbers of both are approximately equal (31 and 35, respectively).

In addition, it is evident from Figure 5 that the essentially uniform latitude distribution of IVCs at lower longitudes differs from that seen at higher longitudes. At higher longitudes the majority of

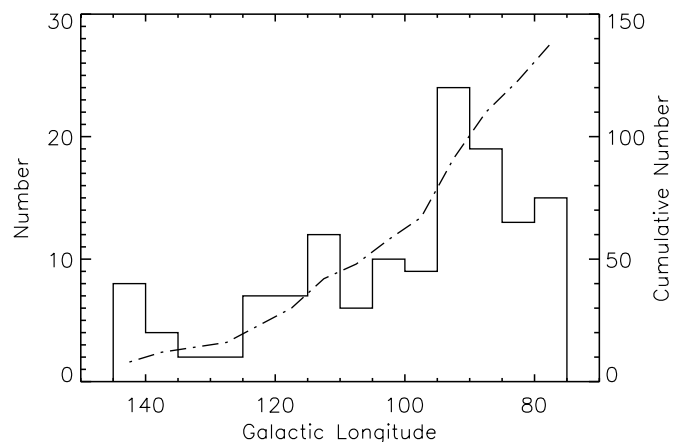


FIG. 6.—Histogram showing the distribution of the detected IVCs with longitude (5° bins). The cumulative distribution is shown by the dot-dashed line (right axis). The majority of the IVCs are found at $l \leq 95^\circ$.

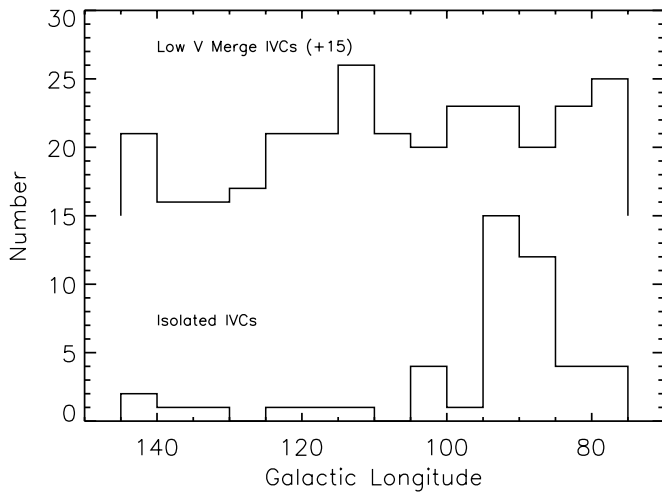


FIG. 7.—Same as Fig. 6, but showing the distribution for the IVCs that merge with allowed H I emission (*top*; offset by 15) and isolated IVCs (*bottom*). Note the fairly uniform distribution of merging IVCs in contrast to the sharp increase in the numbers of isolated IVCs in the lower longitude part of the survey.

the IVCs are clearly associated with local H I emission features that are evident in the LRDS image. Particularly striking is the series of IVCs between $l = 110^\circ$ and 120° and the “chain” of IVCs that runs between $l = 120^\circ$ and 140° at $b \sim +4^\circ$.

In summary, the majority of the IVC sample is characterized by a fairly low deviation velocity and a nonuniform distribution in both longitude and latitude. The majority of the clouds are found at the low-longitude end of the survey. The low-longitude clouds are fairly uniformly distributed in latitude, but the high-longitude clouds tend to follow specific low-velocity local emission features. This, and the change in the relative numbers of merging and isolated IVCs, suggests that there is an enhancement in the frequency of IVC occurrence and a change in their properties at low longitudes in the CGPS.

3.3. Discussion

The global properties of the IVC sample described in the preceding sections can be explained as arising due to a combination of the nature of their origin and the details of Galactic structure in this part of the first and second quadrants of our Galaxy.

First, let us consider the origin of these features and ignore the details of Galactic structure. It is most likely that the majority of the observed IVCs are related to energetic and/or explosive phenomena in the disk of our Galaxy, such as supernova explosions or stellar (cluster) winds. A few extragalactic sources are represented in our catalog (see § 4.1), but it is unlikely that there would be a large population of extragalactic sources matching the observed characteristics of these clouds. Infalling clouds from the halo are also a possible source, but a positive deviation velocity for such objects is not expected in the longitude range of this survey.

Figure 8 shows the expected run of V_{LSR} with heliocentric distance at three longitudes for a flat rotation curve with $R_\odot = 8.5$ kpc and $V_\odot = 220$ km s $^{-1}$. Consider an energetic phenomenon that causes a region of H I to be accelerated such that it obtains a velocity shift of ΔV relative to its original velocity. What is the maximum distance at which the velocity shift is sufficient to make $V_{\text{LSR}} \geq (V_{\text{max}} + 10$ km s $^{-1}$), i.e., we can see the cloud as an IVC? The results for $\Delta V = +20$ and $+50$ km s $^{-1}$ are shown in Figure 8.

There are two points we can take from Figure 8. First, there is the perhaps obvious result that the H I emission associated with

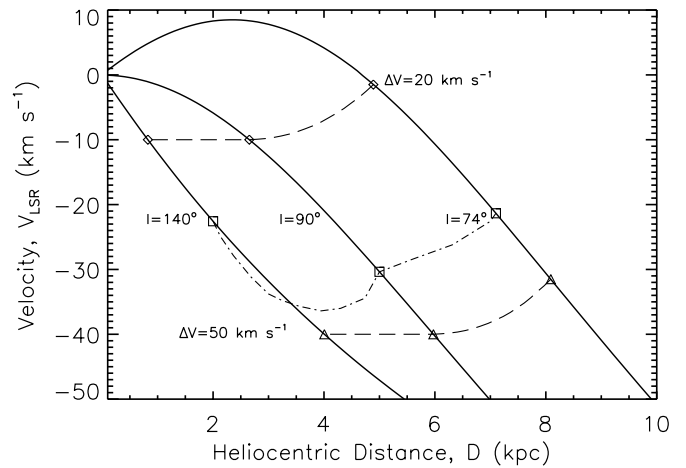


FIG. 8.—Heliocentric velocity curves. The solid curves show V_{LSR} as a function of heliocentric distance at $b = 0^\circ$ for three different longitudes within the survey region. Also shown are the maximum distances at which an H I cloud with $\Delta V = +20$ km s $^{-1}$ (diamonds) and $\Delta V = +50$ km s $^{-1}$ (triangles) would be identified in the survey as an IVC. The dot-dashed line represents the velocity-distance locus of the Perseus arm, not accounting for streaming motions (see text). The distance-velocity points for $l = 74^\circ, 90^\circ$, and 140° are indicated by squares.

more energetic phenomena will be detectable to greater heliocentric distances. For example, an IVC at a distance of 6 kpc at $l = 74^\circ$ with $\Delta V = +20$ km s $^{-1}$ would not show up as an IVC; the velocity-shifted emission would be lost within the allowed emission from H I at 2–3 kpc with $V_{\text{LSR}} \sim +10$ km s $^{-1}$. In contrast, an IVC at the same distance with $\Delta V = +50$ km s $^{-1}$ would have $V_{\text{LSR}} \sim +40$ km s $^{-1}$ and would clearly be detectable as an IVC. The latter would remain distinguishable out to a distance of 8 kpc.

The second point is that as the longitude decreases, the maximum detectable distance of an IVC with a given ΔV increases. For example, IVCs with $\Delta V = +20$ km s $^{-1}$ are only visible out to about 1 kpc at the high-longitude end of the CGPS but could be detected at distances up to about 5 kpc at the low-longitude end of the survey. This second factor may partially explain why we detect more IVCs in the lower longitude sections of the survey: at lower longitudes IVCs can be detected to greater distances and thus sample a larger volume of the Galaxy. It turns out that this tendency is amplified by the known structure and velocity field characteristics of the Galaxy in the survey region.

The phenomena that we assume give rise to IVCs are not uniformly distributed throughout the Galaxy but rather tend to be concentrated in the spiral arms, so the spiral structure of the Galaxy should influence the observed distribution of IVCs. Over the longitude range of the survey we have a relatively good picture of the spiral structure of our Galaxy (see, e.g., Russeil 2003). For our purposes it is sufficient to know that the Sun is located in a local “arm” or “spur,” which is oriented with its long axis pointing toward $l \sim 75^\circ$ and extending in this direction to at least a distance of 4 kpc (Wendker et al. 1991). Beyond this local material the dominant feature at the survey longitudes is the Perseus arm, located at a heliocentric distance of ~ 2 kpc at the high-longitude end of the survey, at ~ 5 kpc at $l = 90^\circ$, and at ~ 7 kpc at the low-longitude end of the survey (using approximate distances from Russeil [2003]). The Perseus arm is far enough from the Sun that there is relatively little difference in the path length through the arm at different longitudes across the survey. In contrast, for the local arm, lines of sight at high longitudes traverse shorter path lengths of arm material (because lines of sight are normal to the long axis of the arm) and increase

as longitudes move through $l = 90^\circ$ to lower longitudes (because lines of sight are parallel to the long axis of the arm).

Given this picture of Galactic structure, we ask, how detectable are IVCs originating from energetic events in the Perseus arm? From Figure 8 it is apparent that only IVCs with fairly high ΔV will be detectable at Perseus arm distances anywhere along the survey. For the outer Galaxy ($l > 90^\circ$) the true situation is actually much worse than it appears in Figure 8, because there are known streaming motions on the order of 30 km s^{-1} between $l \sim 90^\circ$ and 150° (Brand & Blitz 1993; Russeil 2003), probably associated with material entering the spiral arm shock (Roberts 1972). Consider H I gas at $l = 140^\circ$ associated with the Perseus arm. This gas, at a distance of $\sim 2 \text{ kpc}$, should have $V_{\text{LSR}} \sim -20 \text{ km s}^{-1}$ in the simple rotation model. But, due to the streaming motions, the gas actually has a velocity of $V_{\text{LSR}} \sim -50 \text{ km s}^{-1}$, making the detection of IVCs that much more difficult. At lower longitudes streaming motions are not as important, but the distance to the Perseus arm is such that, once again, only the most energetic phenomena are detectable.

In this spiral structure model the volume being probed at the high and low ends of the survey varies by a factor of ~ 64 if we assume that we are just detecting local arm IVCs (a 1 kpc, at most, line of sight changing to a 4 kpc line of sight). If the IVCs were uniformly distributed throughout the arms with a constant density, one would expect to see a comparable increase in the detected numbers; but, as shown in Figure 6, we do not see anywhere close to a factor of 64 increase in the number of detected IVCs at lower longitudes. Thus, we conclude that the IVCs are not uniformly distributed throughout the arm. We note that removing the spiral arm model and just looking at the volume encompassed by a particular velocity cutoff just makes the situation worse. For example, for $\Delta V = 20 \text{ km s}^{-1}$ there is a factor of ~ 200 increase between the high- and low-longitude volumes.

To investigate this in more detail we plot in Figure 9 the distribution of OB associations found within the CGPS, using data from Garmany & Stencel (1992) and Uyaniker et al. (2001), in order to trace the large-scale distribution of star-forming regions and the likely locations for ongoing supernova activity. Using the velocity field of the outer galaxy from Brand & Blitz (1993; which includes streaming motions) we also calculated the detection limit for IVCs with $\Delta V = 20$ and 40 km s^{-1} (equivalent to the $V_{\text{LSR}} = -10$ and -30 km s^{-1} loci for $l \geq 90^\circ$).

First, this picture echoes what was demonstrated in Figure 8, namely, that local arm IVCs are much easier to detect than IVCs from the Perseus arm. Building on this idea, we can explain many of the features of the longitude distribution shown in Figure 6. At low longitudes a 5° wide swath of the survey in longitude will encompass 2–4 OB associations, while at the high-longitude end a similar swath will encounter 0–1 OB associations. This leads to expected changes in the number of detected IVCs per longitude bin on the order of 2–4, which is more in line with the observations compared to the uniform density model. The upturn in IVC numbers at the highest end of the survey might be associated with the Cam OB 1 association. A lack of nearby OB associations contributes to the dearth of IVCs in the range $125^\circ < l < 135^\circ$. The increase and plateau in the range $100^\circ < l < 120^\circ$ is probably associated with the various Cep OB associations. Finally, the large increase at $l \leq 90^\circ$ is due to encountering all of the Cyg OB associations.

The same factors help to explain why the distribution of IVCs with latitude varies across the survey. At low longitudes there is a large total path length (in terms of arm material), so IVCs are numerous enough that they tend to fill all the available latitudes. At higher longitudes the path length is much shorter (tangential

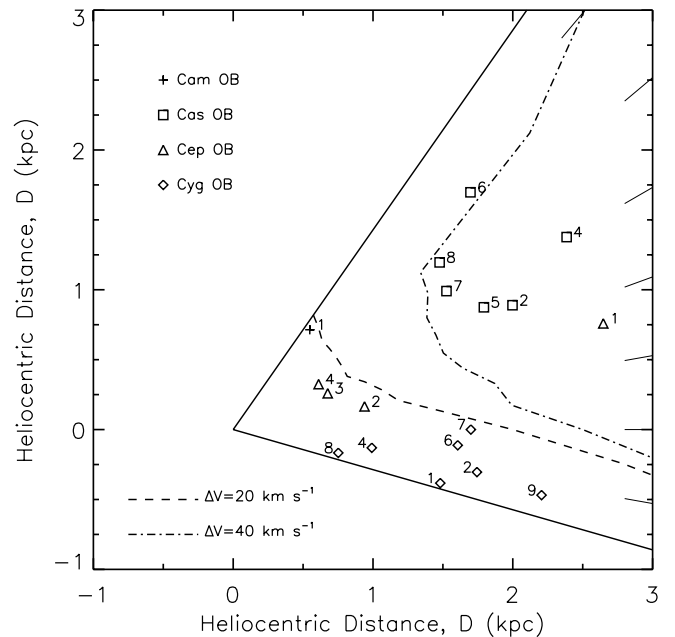


FIG. 9.—OB associations in the CGPS. The approximate limits of the CGPS survey are shown by the solid lines at $l = 75^\circ$ and 150° . OB associations are indicated by the symbols and number labels. The dashed and dot-dashed lines are the detection limits for IVCs with $\Delta V = +20$ and $+40 \text{ km s}^{-1}$, respectively. These limits take into account known streaming motions in this part of the Galaxy. For reference, lines on the right side of the panel indicate $l = 80^\circ$ – 140° at 10° intervals.

to both the local and Perseus arms), and one encounters so few IVCs that latitude filling is impossible.

The global properties of the IVC sample described in this section show that the majority of the detected IVCs are “aware” of the velocity field, spiral structure, and distribution of OB associations in this part of our Galaxy. This is clear evidence that the majority of these features are associated with energetic phenomena occurring within the dense ISM of the Galactic disk. These IVCs thus may ultimately prove to be useful probes of the distribution and history of energetic phenomena occurring in the ISM, particularly in the local arm.

4. INDIVIDUAL IVCs

In this section we present comments on some of the more noteworthy IVCs in our catalog. Two IVCs are associated with known external galaxies. For several IVCs or IVC complexes, we have been able to make possible associations with energetic Galactic phenomena, i.e., supernova remnants (SNRs) and star-forming regions. One IVC is detected in absorption against a background radio continuum source, permitting the derivation of some physical properties for this cloud.

4.1. Known Galaxies

Two of the IVCs in the high-longitude portion of the survey, IVC 7 (IVC 138.5–0.1+41.41) and IVC 10 (IVC 136.5–0.3+40.58), are unusual, as their positions do not correlate with the local H I emission seen at low velocities, and they have spectra that are rising through the high-velocity cutoff of the CGPS. Both of these clouds turn out to be H I emission from relatively nearby spiral galaxies. IVC 10 is H I emission from Maffei 2 (Hurt et al. 1996), and IVC 7 is emission from Dwingeloo 1 (Burton et al. 1996). In the context of this paper these galaxies serve to remind us that, although rare, not all of the IVCs in our sample are necessarily associated with our Galaxy.

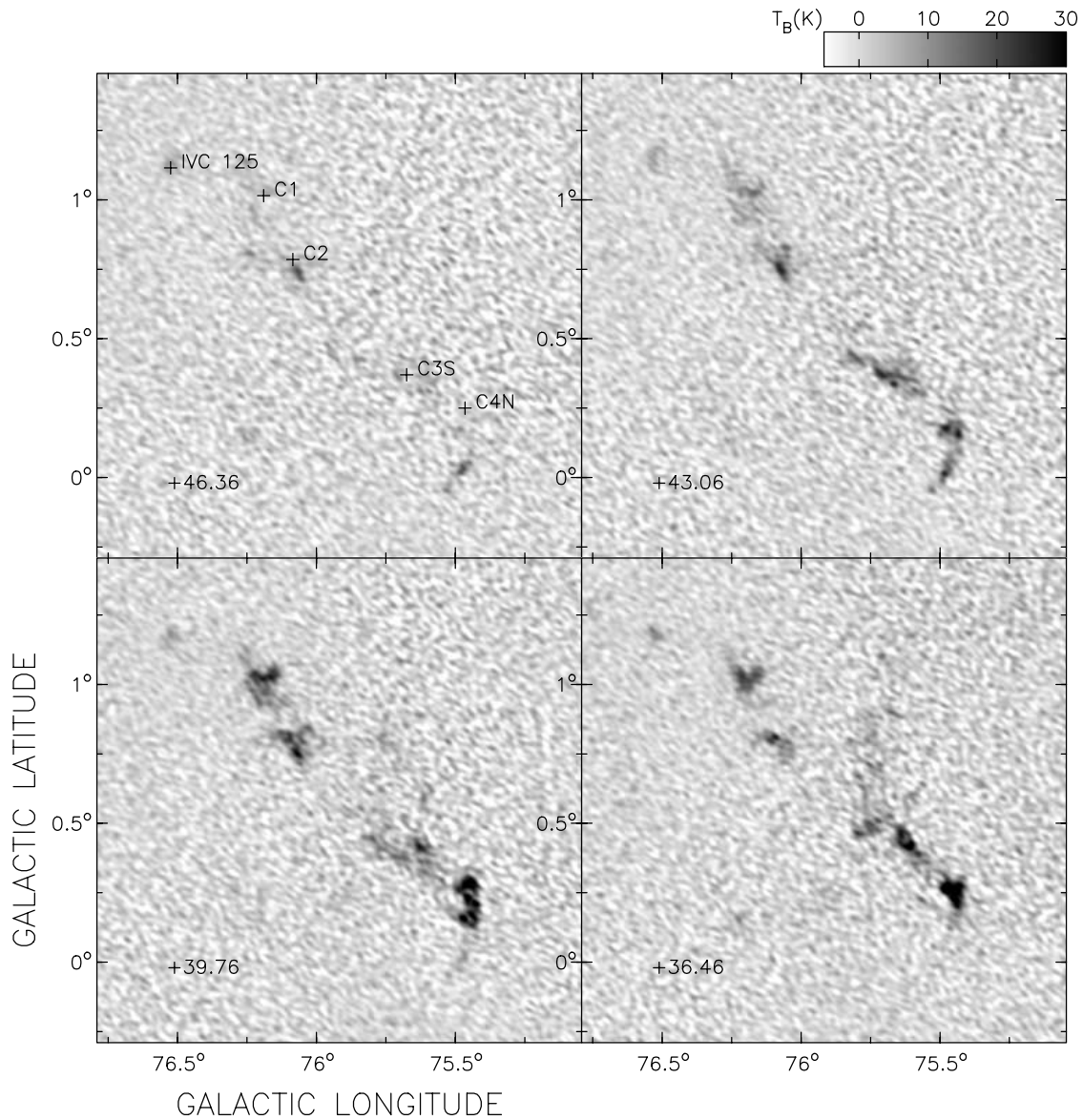


FIG. 10.—Cygnus region clouds. An approximately 1° long chain of IVCs is shown at four different values of V_{LSR} (indicated in the lower left portion of each panel). The objects at $b < 1^\circ$ are probably small H I clouds that have been accelerated by the passage of a SNR shock. IVC 125 has a very broad spectrum and may not be related to the other clouds. The crosses in the top left panel indicate the central position of the average spectra shown in Fig. 11.

4.2. Associations with Supernova Remnants

Accelerated H I emission associated with SNRs can arise either through material that has been swept up by the expanding remnant or due to the encounter of the shock wave with a discrete H I cloud (e.g., Landecker et al. 1980). Confident association of a specific H I feature with a known SNR is difficult and rests primarily on some morphological similarity (or even just a positional coincidence) between the remnant as seen at other wavelengths and the observed H I emission (see, e.g., Routledge et al. 1991).

With this in mind we compared the positions of the detected IVCs with a listing of known SNRs (Green 2004) and found that a few IVCs are located near known SNRs. IVC 13 (IVC 131.0+3.2+13.38) and IVC 106 (IVC 84.1–0.6+44.71) are each located about $0^\circ.25$ away from SNRs 3C 58 and G84.2–0.8, respectively. IVC 111 (IVC 85.5+0.9+49.65) is coincident with part of the shell of SNR G85.4+0.7 as seen in the 1420 MHz continuum. This IVC is also a very faint object whose spectrum extends beyond the high-

velocity cutoff of the survey. Finally, IVC 98 (IVC 88.8+4.9+19.97) is located within the extent of HB 21 as seen in the continuum at 1420 MHz.

In their study of SNR G78.2+2.1 (the so-called γ Cygni SNR) Landecker et al. (1980) discovered four high-velocity features that they termed H I “bullets.” As the clouds were located within the boundaries of the SNR as viewed in the radio continuum, they modeled these features as H I clouds that had been overrun and accelerated by the SNR shock wave. One of their clouds (IIa) is IVC 134 (IVC 78.0+1.9+48.83); the other positive velocity clouds in their paper lie outside the velocity range of our survey. All of the clouds are about $10'$ in size and have $\Delta V_{\text{FWHM}} \sim 10 \text{ km s}^{-1}$. Cloud IIa has a mass of about $20 M_\odot$, while the other three clouds have masses around $4\text{--}6 M_\odot$ (all masses were calculated assuming optically thin H I emission and a distance of 1 kpc).

One of the more striking features observed in the low-longitude end of the survey is the group of IVCs shown in Figure 10, which we have denoted IVC complex 10. This $\sim 1^\circ$ long chain of bright IVCs is immediately apparent in the high-velocity channels in this

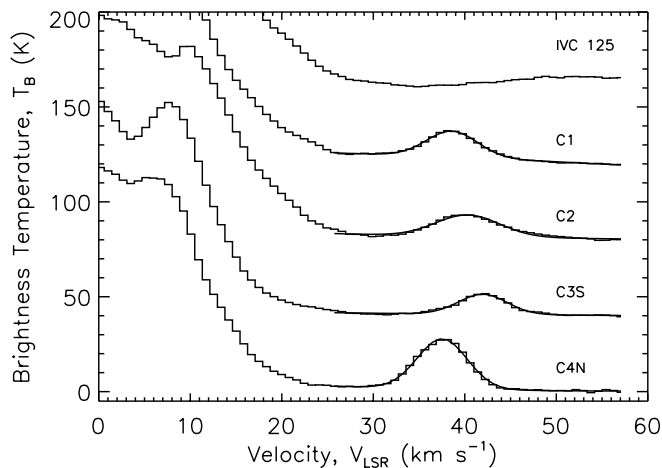


FIG. 11.—Cygnus region spectra. Spatially averaged spectra taken around the locations labeled in Fig. 10 are shown with offsets of 40 km s^{-1} between each spectrum. Note the very broad spectrum of IVC 125, which apparently continues beyond the high-velocity limit of the survey. Gaussian fits to the four lower IVC features are also shown (solid curves).

region. Figure 11 shows spatially averaged spectra obtained at the points indicated in Figure 10. (Fig. 11 includes the spectrum of nearby IVC 125 [IVC 76.5+1.1+52.13], which is rising through the high-velocity limit of the survey.) All of the clouds are kinematically distinct from the bulk of the Galactic H I emission. Gaussian velocity fits were obtained to the four clouds of complex 10, and all had fitted FWHMs between 6 and 8 km s^{-1} . Using these spectra and assuming optically thin emission, we determined that the clouds have masses between $4D^2$ and $6D^2 M_{\odot}$ (where D is the distance in kiloparsecs). All of the complex 10 clouds are of the order of $10'$ in size and have deviation velocities of the order of $+30 \text{ km s}^{-1}$, placing them toward the high end of the deviation velocity distribution (see Fig. 3). Unlike the case of IVC 134 there is no SNR visible at radio wavelengths that can be associated with these objects, but otherwise they are very similar in their properties to the small-scale features discussed in Landecker et al. (1980), and a similar origin is possible.

IVCs may also be related to the final stages of the evolution of a SNR, in which the SNR is dissipating into the general ISM and may only be visible as accelerated H I emission. A possible example of such a merger-stage SNR is described in Higgs et al. (2001; IVC 69 in this survey). Associated with this possible merger-stage SNR are a number of small-scale intermediate-velocity H I features termed “knots” by the authors. These knots have typical sizes of a few arcminutes, velocity profiles with $\text{FWHM} \sim 4\text{--}8 \text{ km s}^{-1}$, and H I masses of $\sim 1D^2 M_{\odot}$. We note that IVC 70 (IVC 91.0–2.6+36.46) and IVC 92 (IVC 90.7–2.5+42.23) are knots 8 and 10, respectively, of Higgs et al. (2001).

Finally, we examined our entire sample to see whether there was any indication that the IVCs were associated positionally with known SNRs. Using the SNR catalog of Green (2004) we calculated the offset between the position of each IVC in our sample and the nearest cataloged SNR, then repeated the calculation for a random sample of positions. The two distributions of offsets were found to be statistically identical using a Wilcoxon rank sum test and an F -variance test on the mean and standard deviations of the distributions, respectively. There could be a number of not mutually exclusive reasons for this result, including that a significant number of the IVCs are not accelerated by SNRs, that the SNR catalog (known to be incomplete) is missing the associated SNRs, and that many of the SNRs are very old and the H I emission itself is all that remains.

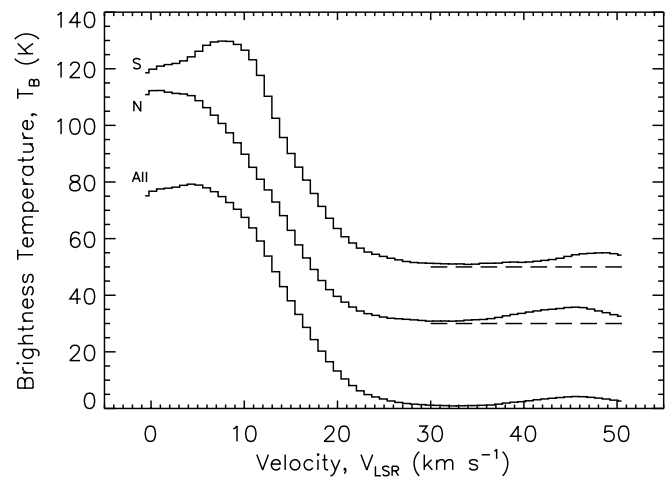


FIG. 12.—IVC 105 spectra. The spatially averaged spectra of IVC 105 illustrate the velocity structure of the cloud. The southern spectrum (S) was centered at $l = 84^{\circ}55$, $b = -0^{\circ}230$, the northern spectrum (N) at $l = 84^{\circ}415$, $b = 0^{\circ}145$, and the average spectrum for the entire cloud (All) at $l = 84^{\circ}460$, $b = -0^{\circ}035$. Note how the southern spectrum clearly extends beyond the high-velocity cutoff.

4.3. Associations with Star Formation Regions

Another means to accelerate H I is through the action of regions of star formation. Expanding H I shells, formed through photodissociation of surrounding molecular gas, are known to occur around H II regions and have velocity shifts of the order of tens of kilometers per second (Kotthes & Kerton 2002). High-velocity neutral material is also known to be associated with outflows from some star-forming regions, such as the strong neutral outflow from DR 21 (Russell et al. 1992). One interesting example of an IVC that appears to be associated with a star-forming region is IVC 105 (IVC 84.5–0.1+47.18). This IVC is one of a few in our survey that have emission extending beyond the high-velocity cutoff of the CGPS data (see Fig. 12).

Bally & Reipurth (2003) used wide-field [S II] and H α images to detect a number of Herbig-Haro (HH) objects in the nearby ($D \sim 600 \text{ pc}$) Pelican Nebula around $l = 84^{\circ}5$, $b = 0^{\circ}$ (see Fig. 13). In one case (HH 555) [S II] spectra were also obtained at Keck I, and a blueshifted outflow with velocities up to -85 km s^{-1} was detected. The relatively lower angular resolution of our observations makes it impossible to directly associate IVC 105 with any particular HH object, and the large spatial extent of IVC 105 also argues against such a specific association. We suggest that IVC 105 is accelerated neutral material associated with the general high level of star formation–driven outflow going on in the region, as signposted by the presence of the numerous HH objects. If IVC 105 is at the distance of the Pelican Nebula, an (absolute) velocity shift of the order of what is observed for the HH 555 outflows would easily shift the H I emission to the observed velocity. Using the average spectra shown in Figure 12 and assuming a distance of 600 pc , we find that the IVC has a mass of about $20 M_{\odot}$.

4.3.1. An IVC Seen in H I Absorption

IVC 75 (IVC 91.2+1.7+27.39) is an elongated ($\sim 0^{\circ}7 \times 0^{\circ}085$ in angular size), kinematically isolated IVC visible at velocities of $+26 \text{ km s}^{-1} \leq V_{\text{LSR}} \leq +30 \text{ km s}^{-1}$. What makes this IVC of particular interest is that it crosses over a strong compact continuum source (G91.11+1.58) that is part of the more extended BG 2107+49 complex (see Fig. 14). This unusual complex was suggested by Higgs et al. (1987) to be a Galactic massive star-forming region at a distance of $\sim 10 \text{ kpc}$. The detection of 6.7 GHz

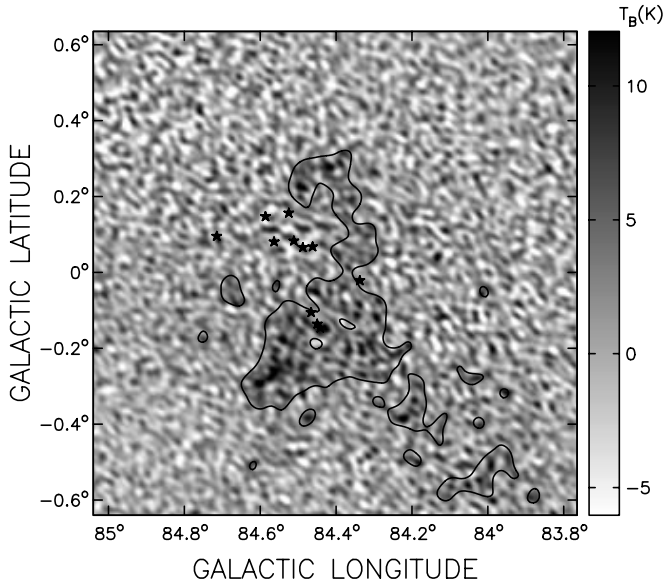


FIG. 13.—IVC 105 at $V_{\text{LSR}} = +50.48 \text{ km s}^{-1}$. Contours are at $T_B = 2.5 \text{ K}$ for the same image smoothed to $\sim 3'$ resolution. Stars indicate the positions of HH objects described by Bally & Reipurth (2003).

methanol maser emission at $V_{\text{LSR}} = -70 \text{ km s}^{-1}$ from the *IRAS* point source IRAS 21074+4949 (Szymczak et al. 2000), which is located within the radio nebosity $\sim 12'$ from G91.11+1.58, supports the star formation region interpretation. Radio recombination lines have been detected from BG 2107+49 at a velocity of -80 km s^{-1} . The very large difference in radial velocity between IVC 75 and BG 2107+49 makes their direct association very unlikely.

IVC 75 is seen in absorption against G91.11+1.58. We believe this is the first detection of H I 21 cm absorption by an IVC. Using standard techniques (e.g., Normandeau 1999) we were able to derive an optical depth of $\tau = 0.25 \pm 0.05$ and a spin temperature of $T_s = 32 \pm 8 \text{ K}$ for the IVC (both are averages across the absorption-line profile). A more sophisticated analysis of the combined emission-absorption spectrum using the technique

described by Dickey et al. (2003) results in a measurement of the spin temperature in the cold neutral medium (CNM) component of IVC 75 of $T_{\text{CNM}} = 30 \pm 2 \text{ K}$. The similarity between the first spin temperature (which is a column-density-weighted harmonic mean of all temperature components) and the CNM component temperature suggests that the H I emission of IVC 75 is due almost entirely to cold material, implying that this IVC is primarily composed of cold gas. The mass of IVC 75 is $9D^2 M_{\odot}$, or $\leq 900 M_{\odot}$ using the kinematic distance of the continuum source ($\sim 10 \text{ kpc}$) as an upper limit. However, we suggest below that the distance to this IVC may be much less, $\sim 100 \text{ pc}$.

We can obtain a rough estimate of the distance to this IVC by assuming that the CNM material we detect in absorption is in thermal pressure equilibrium with the surrounding ISM and assuming a shape for the IVC. One can relate the thermal ISM pressure (P/k , in units of K cm^{-3}) and the heliocentric distance (D) by the expression

$$P/k = \frac{N_{\text{H}} T_s}{D \theta}, \quad (1)$$

where k is the Boltzmann constant, T_s is the spin temperature, N_{H} is the opacity-corrected column density, and θ is the angular width of the IVC ($\theta = 0.085$ for IVC 75). The expression assumes that the line-of-sight depth of the IVC is equal to its width (i.e., a cylindrical geometry). From our observations the opacity-corrected column density is $N = 4.69 \times 10^{19} \text{ cm}^{-2}$ and $T_s \sim 30 \text{ K}$. Using these values we can write equation (1) as

$$P/k = \frac{261(T_s/30 \text{ K})}{(D/\text{kpc})(\theta/0.1)}. \quad (2)$$

Wolfire et al. (2003) estimate that the typical thermal pressure in the Galactic plane follows an exponential expression,

$$P/k = 1.4 \times 10^4 \exp(-R/R_0), \quad (3)$$

where R is the galactocentric distance in kiloparsecs and $R_0 = 5.5 \text{ kpc}$. For $l = 91^\circ$ equations (2) and (3) agree at a heliocentric

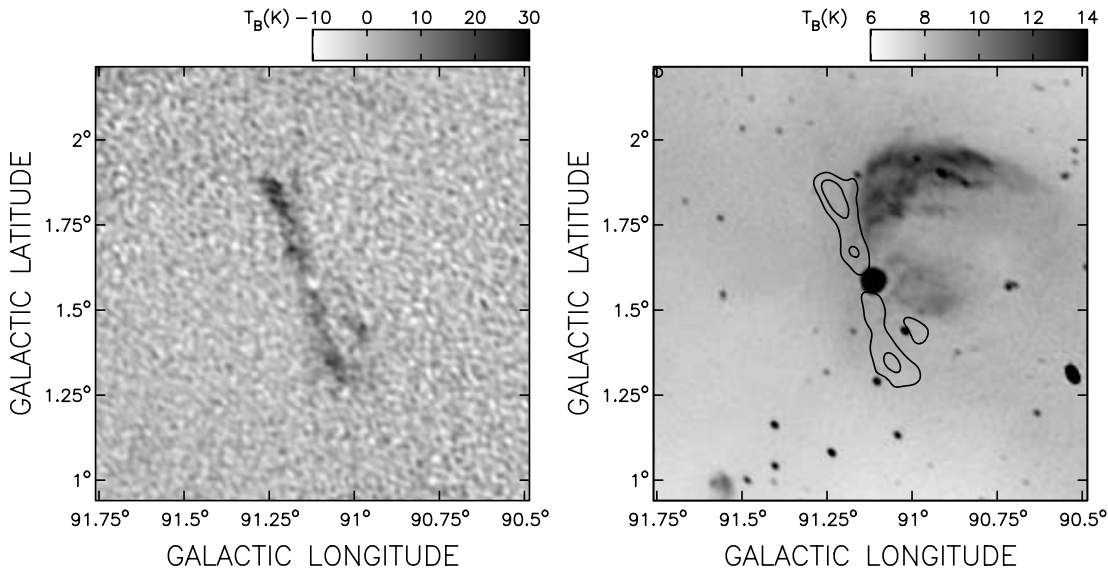


FIG. 14.—Continuum absorption by an IVC. IVC 75 is a filamentary IVC distributed symmetrically around a thermal point source associated with BG 2107+49. The left panel shows the IVC at $V_{\text{LSR}} = 27.39 \text{ km s}^{-1}$, with the continuum absorption showing up as a white area near the center of the IVC. The right panel shows 1420 MHz continuum emission of the same region overlaid with H I contours (smoothed to $3'$ resolution).

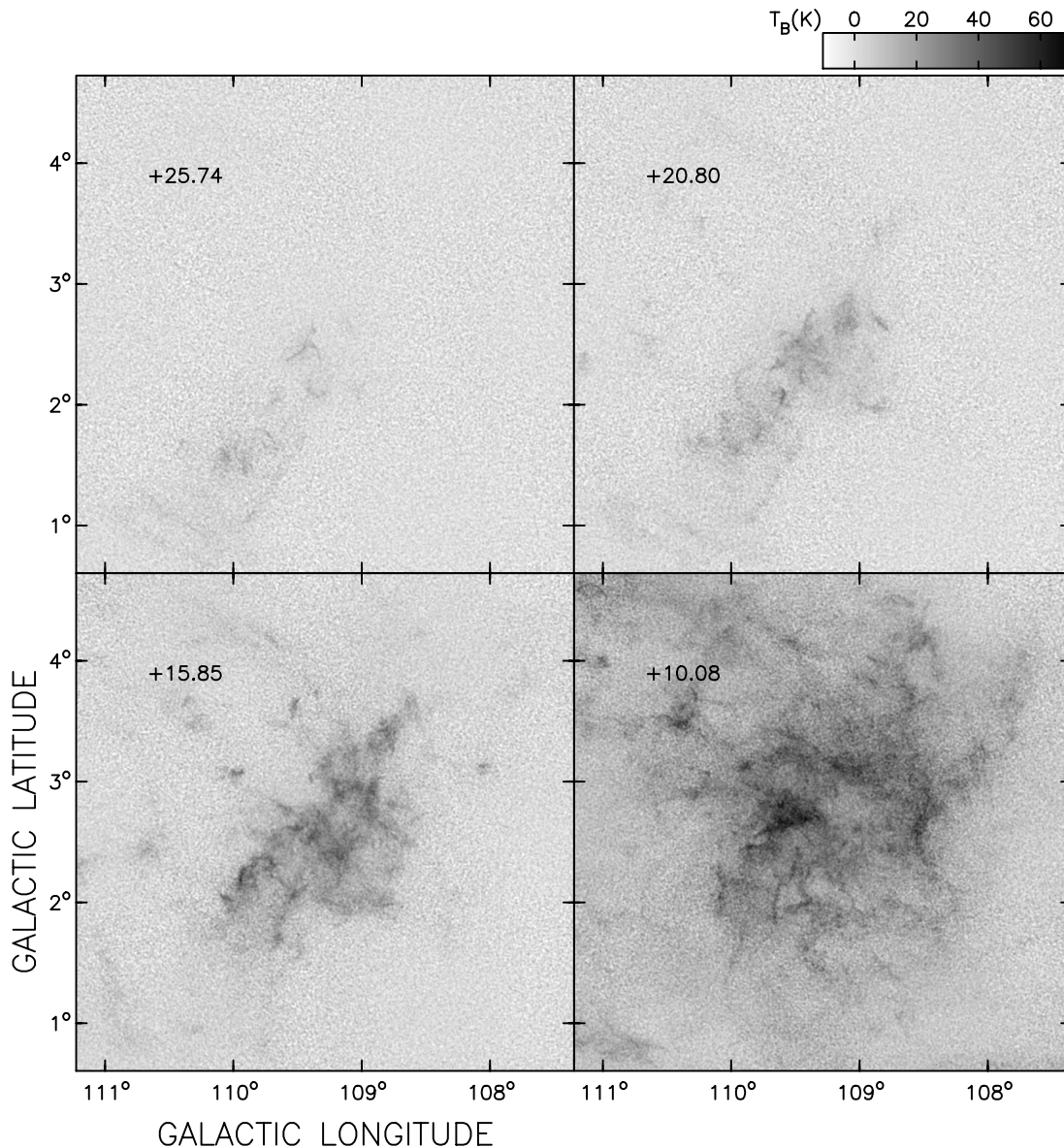


FIG. 15.—Nearby H I IVC complex. Shown is a large H I complex that is probably at a distance of ~ 1 kpc. The V_{LSR} of each velocity channel is indicated in the upper left corner of each panel. At lower resolution this feature stands out because of its high deviation velocity for its longitude, but the wealth of intricate details visible in this high-resolution view are lost.

distance of $D = 0.1$ kpc. Equation (3) implies that at this Galactic longitude, pressure has a very weak dependence on heliocentric distance. If we vary D from 0 to 10 kpc ($8.5 \text{ kpc} \leq R \leq 13.2 \text{ kpc}$), P/k varies only from 3000 to 1300 K cm^{-3} , respectively. In contrast, the D^{-1} dependence in equation (2) means that the pressure required for pressure equilibrium drops off much more rapidly with increasing D . It seems clear that if the object is in pressure equilibrium, it must be a fairly local object. It is interesting to note that, if at a distance of 100 pc, this IVC is near the boundary of the Local Bubble in this direction (Lallement et al. 2003).

At this distance the IVC would have a mass of $\sim 0.1 M_{\odot}$, and overall it would be similar in temperature, optical depth, and mass to the “local filament” H I self-absorption (HISA) feature examined by Gibson et al. (2000). If this IVC had not been velocity-shifted away from the bulk of the H I emission, it potentially could have been seen as a HISA feature. It is noteworthy that HISA clouds are also thought to be dominated by cold H I,

and many have filamentary structure similar to that of IVC 75 (Gibson et al. 2005).

4.4. IVC Complexes

In addition to the smaller, arcminute-scale IVCs, we also identified 13 spatially large (degree-scale) IVC structures. These larger complexes are typically seen as “blobs” in the lower resolution LRDS. One complex (G109.5+2.5; see Fig. 15) is the high-velocity, low-longitude part of the emission that can be seen stretching from $l \sim 110^{\circ}$ to 120° in the background LRDS velocity slice shown in Figure 5. The relatively high deviation velocity of the complex makes it quite striking even at the lower resolution of the LRDS, first becoming detectable around $+25 \text{ km s}^{-1}$. The essentially featureless blob seen in the LRDS gives way to an intricate morphology of overlapping filamentary structures and compact regions of bright H I emission in the high-resolution data. By the $+10.08 \text{ km s}^{-1}$ velocity channel, the structure starts to become overwhelmed by local allowed emission, but

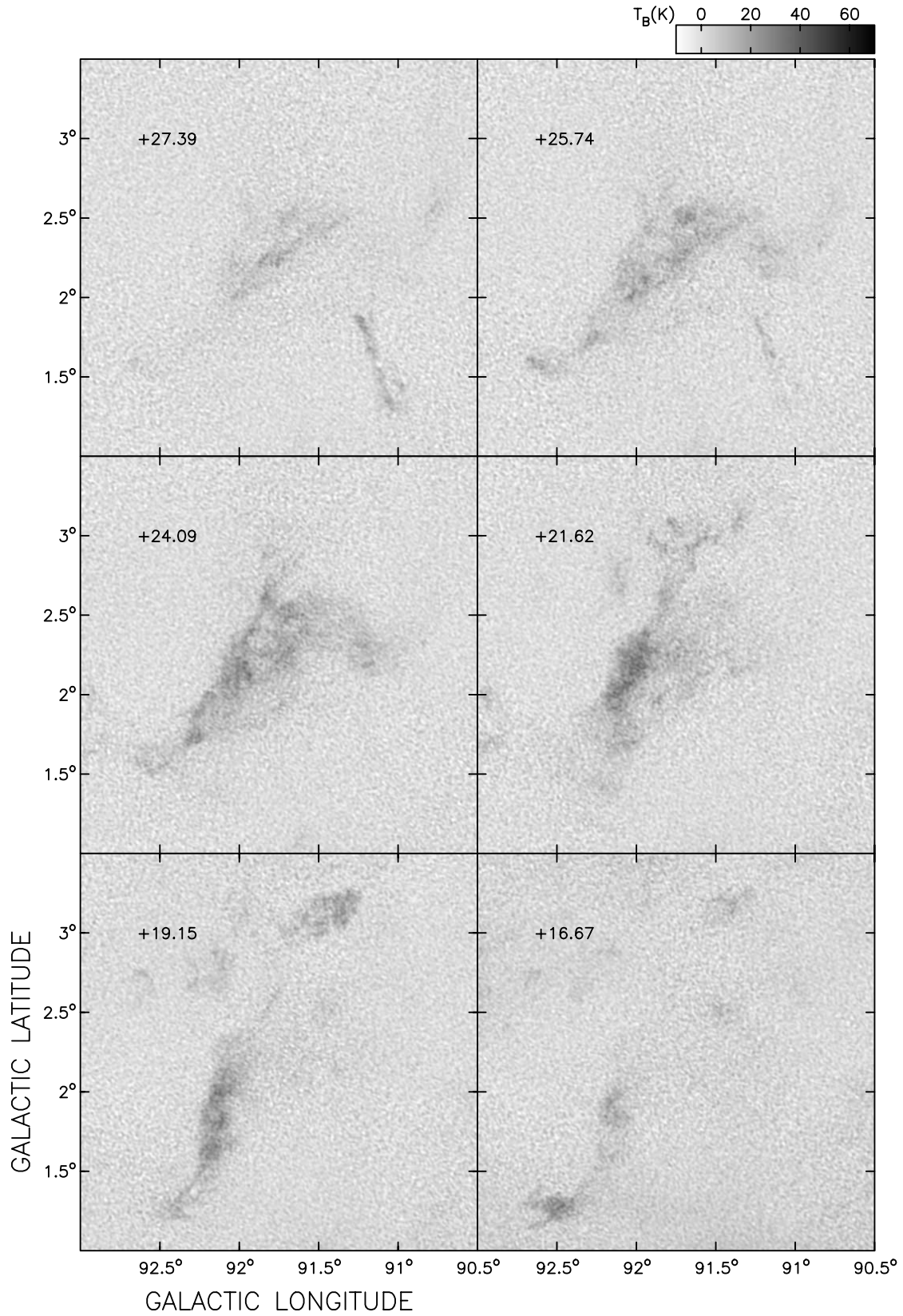


FIG. 16.—Distant H I complex. This complex is probably much more distant than the complex shown in Fig. 15, with a distance of at least 5 kpc being likely. The V_{LSR} of each velocity channel is indicated in the upper left corner of each panel, and the interesting velocity structure of the complex is apparent.

one can follow certain morphological features for a few velocity channels further before the structure is completely lost. The edge of the complex around $l = 110^\circ$, $b = 2^\circ$ appears to be associated with the Sh 2-155 H II region at a distance of 0.9 ± 0.3 kpc (Foster & Routledge 2003). Using a distance of 1 kpc and looking just at the emission in the ranges $109^\circ \leq l \leq 110^\circ$ and $2^\circ \leq b < 3^\circ$ with $V_{\text{LSR}} \geq +10.08$ km s $^{-1}$, we find $M \sim 1300 M_\odot$. To give an idea of the physical scale of the complex, the long axis of the emission seen in the $+15.85$ km s $^{-1}$ channel is about 45 pc in length.

Another interesting complex, notable for both its size and velocity structure, is located around $l = 92^\circ$, $b = +2.2$ (see Fig. 16). As in the previous complex, it has a high deviation velocity and first becomes apparent around $+27$ km s $^{-1}$. By $+21$ km s $^{-1}$ the complex has compressed in longitude and has emission maxima that extend both southward and northward until fading away at lower velocities. We do not have a distance estimate for the complex. Its emission appears to be smoother than that of G109.5+2.5, perhaps implying that the former is more distant. Foster et al. (2004) describe a nearby (at $l \sim 93^\circ$) region of fairly recent star-forming and supernova activity at a distance of ~ 5 kpc. Based on their work it seems that a reasonable upper limit for energetic activity along this line of sight might be ~ 10 kpc. The $\sim 1^\circ$ long region of emission at $l = 92^\circ$ has a mass of $120D^2 M_\odot$ or $10^{3.5} M_\odot \leq M \leq 10^{4.1} M_\odot$ and a physical length of 90–180 pc using the two limits of 5 and 10 kpc, respectively.

5. SUMMARY AND CONCLUSIONS

We have examined the CGPS Phase I H I data for positive velocity IVCs and cataloged 138 IVCs and 13 IVC complexes. The spatial distribution of the IVCs supports the idea that these are primarily objects associated with energetic events within the Galaxy and not a lower velocity version of HVCs. Most of the IVCs we catalog are likely to be relatively local phenomena in the local spiral arm and thus provide the opportunity to map out the distribution and history of energetic ISM events in the solar vicinity. Tentative associations between a few IVCs and SNRs or star-forming regions are suggested. We suggest that careful multiwavelength investigations of the environs of IVCs hold promise for further progress in this direction.

A few of the IVCs have spectra that apparently continue beyond the high-velocity cutoff of the survey. Two of these objects are known galaxies, illustrating that, although rare, not all of the IVCs are necessarily Galactic objects. One of the IVCs (105) is apparently associated with a region of active outflows from newly formed stars in the Pelican Nebula. Spectra of one of these outflows indicate outflow velocities of magnitude sufficient to create the observed IVC.

A number of the smaller scale IVCs may be shocked H I bullets of material similar to those first discussed in Landecker et al. (1980). Such objects appear to be fairly common in the lower longitude portion of the survey, with complex 10 being a particularly striking example. Supernovae are a likely origin for the acceleration of these IVCs. Some of the other IVCs (e.g., IVC 69) may be related to the actual merger stage of a SNR.

In one case (IVC 75) we were able to determine the optical depth and spin temperature of the IVC from radio continuum absorption measurements. This is the first 21 cm absorption-line measurement of an IVC. Interestingly, the IVC turns out to be primarily cold H I and, apart from its large velocity shift, appears similar to permitted-velocity small HISA clouds. We suggest this IVC may be located near the edge of the Local Bubble.

Finally, we present two examples of large degree-scale features. These complexes span many tens of parsecs in linear scale and have masses in the 10^3 – $10^4 M_\odot$ range. We suggest they provide an opportunity to study the intricate structure of the ISM in the plane of our Galaxy free of the confusion that typifies permitted-velocity clouds. The extent to which they can be used for this purpose will depend on the degree to which the physical state (molecular, atomic, or ionized), morphology, and internal kinematics are disturbed by the processes that caused them to become IVCs. Our current view that the Galactic ISM as a whole is shaped by energetic events suggests the possibility that there may well be significant similarities between low-latitude IVCs and permitted-velocity clouds. We plan to both continue our search for these structures in the expanding CGPS database and explore some of the more intriguing IVCs, such as the large complexes, in more detail, taking advantage of this relatively uncluttered view of the H I emission in the disk of our Galaxy.

A. J. S. thanks the University of British Columbia Science Co-op Programme for supporting his work term at the Dominion Radio Astrophysical Observatory (DRAO), during which this research project was begun. The DRAO Synthesis Telescope is operated as a national facility by the National Research Council of Canada. The Canadian Galactic Plane Survey is a Canadian project with international partners and is supported by grants from the Natural Sciences and Engineering Research Council of Canada. Data from the Canadian Galactic Plane Survey are publicly available through the facilities of the Canadian Astronomy Data Centre (<http://cad.c.hia.nrc.ca>). The authors were Guest Users at the Canadian Astronomy Data Centre, which is operated by the Herzberg Institute of Astrophysics, National Research Council of Canada. This research is partially supported through a grant from Iowa State University.

REFERENCES

- Bally, J., & Reipurth, B. 2003, *AJ*, 126, 893
 Brand, J., & Blitz L. 1993, *A&A*, 275, 67
 Burton, W. B., Verheijen, M. A. W., Kraan-Korteweg, R. C., & Henning, P. A. 1996, *A&A*, 309, 687
 Dickey, J. M., McClure-Griffiths, N. M., Gaensler, B. M., & Green, A. J. 2003, *ApJ*, 585, 801
 Foster, T., & Routledge, D. 2003, *ApJ*, 598, 1005
 Foster, T., Routledge, D., & Kothes, R. 2004, *A&A*, 417, 79
 Garmany, C. D., & Stencel, R. E. 1992, *A&AS*, 94, 211
 Gibson, S. J., Taylor, A. R., Higgs, L. A., Brunt, C. M., & Dewdney, P. E. 2005, *ApJ*, 626, 195
 Gibson, S. J., Taylor, A. R., Higgs, L. A., & Dewdney, P. E. 2000, *ApJ*, 540, 851
 Green, D. A. 2004, *Bull. Astron. Soc. India*, 32, 335
 Higgs, L. A., Kerton, C. R., & Knee, L. B. G. 2001, *AJ*, 122, 3155
 Higgs, L. A., & Tapping, K. F. 2000, *AJ*, 120, 2471
 Higgs, L. A., Vallée, J., Albinson, J. S., Batrla, W., & Goss, W. M. 1987, *A&A*, 181, 351
 Hurt, R. L., Turner, J. L., & Ho, P. T. P. 1996, *ApJ*, 466, 135
 Kothes, R., & Kerton, C. R. 2002, *A&A*, 390, 337
 Lallement, R., Welsh, B. Y., Vergely, J. L., Crifo, F., & Sfeir, D. 2003, *A&A*, 411, 447
 Landecker, T. L., Roger, R. S., & Higgs, L. A. 1980, *A&AS*, 39, 133
 Landecker, T. L., et al. 2000, *A&AS*, 145, 509
 Normandeau, M. 1999, *AJ*, 117, 2440
 Putman, M. E., & Moore, B. 2002, in *ASP Conf. Ser. 276, Seeing Through the Dust*, ed. A. R. Taylor, T. L. Landecker, & A. G. Willis (San Francisco: ASP), 127
 Roberts, W. W., Jr. 1972, *ApJ*, 173, 259
 Routledge, D., Dewdney, P. E., Landecker, T. L., & Vaneldik, J. F. 1991, *A&A*, 247, 529

- Russeil, D. 2003, *A&A*, 397, 133
- Russell, A. P. G., Bally, J., Padman, R., & Hills, R. E. 1992, *ApJ*, 387, 219
- Szymczak, M., Hrynek, G., & Kus, A. J. 2000, *A&AS*, 143, 269
- Taylor, A. R., et al. 2003, *AJ*, 125, 3145
- Uyaniker, B., Furst, E., Reich, W., Aschenbach, B., & Wielebinski, R. 2001, *A&A*, 371, 675
- Wakker, B. P. 1991, *A&A*, 250, 499
- . 2004, in *High-Velocity Clouds*, ed. H. van Woerden et al. (Dordrecht: Kluwer), 25
- Wendker, H. J., Higgs, L. A., & Landecker, T. L. 1991, *A&A*, 241, 551
- Wolfire, M. G., McKee, C. F., Hollenbach, D., & Tielens, A. G. G. M. 2003, *ApJ*, 587, 278